Appl. Phys. B 81, 945–953 (2005)
DOI: 10.1007/s00340-005-2012-1

Applied Physics B
Lasers and Optics

M. SCHULZ-RUHTENBERG[1]
I.V. BABUSHKIN[1,2]
N.A. LOIKO[2]
T. ACKEMANN[1,4,✉]
K.F. HUANG[3]

Transverse patterns and length-scale selection in vertical-cavity surface-emitting lasers with a large square aperture

[1] Institut für Angewandte Physik, Westfälische Wilhelms-Universität Münster, Corrensstraße 2/4, 48149 Münster, Germany
[2] Institute of Physics, Academy of Sciences of Belarus, Prospekt Nezavisimosti 68, 220072 Minsk, Belarus
[3] Department of Electrophysics, National Chiao Tung University, Hsinchu, Taiwan
[4] Department of Physics, University of Strathclyde, 107 Rottenrow, Glasgow G4 0NG, Scotland, UK

Received: 20 May 2005/Revised version: 2 September 2005
Published online: 5 November 2005 •

ABSTRACT The length-scale selection in complex emission patterns spontaneously arising in broad-area vertical-cavity surface-emitting lasers is studied experimentally. The wavenumbers of individual tilted wave modes show a square-root-like dependence on the detuning between emission frequency and longitudinal cavity resonance, in accordance with theoretical expectations. The absolute values of the wavenumbers are in good qualitative agreement with calculations taking into account the reflection properties of the Bragg reflectors and dispersion.

PACS 42.60.Jf; 42.65.Sf; 42.55.Sa; 42.55.Px

1 Introduction

Vertical-cavity surface-emitting lasers (VCSELs) are an attractive type of semiconductor laser with a rather special design: typically three quantum wells (QWs) are incorporated in the middle of a spacer layer with a thickness of one wavelength, which is sandwiched on both sides by highly reflective Bragg mirrors (see e.g. Refs. [1, 2]). As a result, they operate intrinsically in single-longitudinal mode and typically the emitted beam is non-astigmatic and has a rather low divergence. Hence, their beam quality is superior to those of conventional edge-emitting Fabry–Perot-type semiconductor lasers, at least if they operate in the fundamental spatial mode.

However, due to the thinness of the gain medium (typically only 25 nm) the output power of a VCSEL is limited; e.g. for devices with a diameter of a few micrometers operating in single fundamental transverse mode this is about a mW [3]. Hence, if a high output power is desired, VCSELs need to be produced with a large extent in the transverse direction. High-power devices are desirable for material treatment, laser pumping, free-space communication and medical applications; see e.g. Ref. [4]. These VCSELs tend to operate in a transversely modulated state (see e.g. Refs. [5–10]). This is undesirable, of course, for many applications since it reduces the beam quality and in the case of the excitation of non-degenerate transverse modes also the temporal coherence. On the other hand, it makes broad-area VCSELs very attractive for studies of the spontaneous formation of spatial patterns in optics.

The selection of the spatial structure emerging at threshold is determined by an interplay of the spatial and spectral properties of the transverse modes of the cavity and the spectral and possibly spatial gain and loss profiles. The mode (or a family of degenerate modes) with the highest linear (i.e. unsaturated) net gain (gain minus losses) becomes unstable at threshold. This can be formalized by a linear stability analysis of the zero, non-lasing reference state, against a suitably chosen set of functions, usually the eigenmodes of the cavity. In the case of a plano-planar cavity with an infinite extent (or some forms of rectangular boundary conditions), the eigenmodes are simply transverse Fourier modes. It is this limit which theoretical studies of the spontaneous formation of self-organized patterns in lasers and other nonlinear optical cavities (see e.g. Refs. [11–15]) tend to concentrate on and, indeed, the cavity design of VCSELs meets quite well the assumptions of a single-longitudinal mode, plano-planar resonator with high quality factor used in these works. These transverse Fourier modes represent plane waves traveling at an angle to the optical axis. Hence, they are often denoted as 'tilted waves' [14]. The selection of the tilt angle can be understood in quite simple terms from the resonance condition in plano-planar cavities: a plane wave traveling on-axis ($q = 0$) is resonant if a multiple of half a wavelength matches the cavity length L (assuming a Fabry–Perot resonator), i.e. if $k_0 2L = 2\pi m$. If the optical frequency ω_0 (and thus the wavenumber k_0) is larger than the resonant frequency ω_c (wave vector $\boldsymbol{k}_c$) for on-axis radiation, the resonance condition can be re-established for a wave which is tilted with respect to the optical axis, since the projection of the wave vector on the optical axis has a smaller length (Fig. 1).

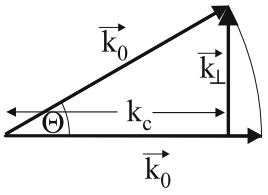

FIGURE 1 Resonance condition in a plano-planar cavity and tilted waves

✉ Fax: +44-141 552 2891, E-mail: thorsten.ackemann@strath.ac.uk

The transverse wave vector $\boldsymbol{k}_\perp \approx \Theta k_0$ of the resonant tilted wave can be obtained from the condition for the phase mismatch

$$\delta\varphi = (k_0 - k_c)2L = \frac{k_\perp^2}{2k_0}2L\,, \tag{1}$$

which can be derived from the construction depicted in Fig. 1 (in the paraxial limit). Thus, if the optical frequency is higher than the cavity resonance, tilted waves with $k_\perp > 0$, i.e. patterned states, will be selected; if the optical frequency is lower than the cavity resonance the homogeneous state is the most favored one.

We mention that although the length-scale selection is obtained in linear order (as in most pattern-forming systems; see e.g. Ref. [16]), the resulting spatial structure is a nonlinear dissipative structure, since nonlinear effects are responsible for the saturation of the linearly unstable structure at finite amplitude and the selection of the emerging pattern consisting usually only of a subset of all degenerate (or nearly degenerate) linearly unstable modes (see e.g. Refs. [11–15, 17]).

After early investigations in VCSELs yielded Gauss–Laguerre- or Gauss–Hermite-like modes in spite of the nominally plano-planar cavity geometry (being distorted due to effects like thermal lensing; see e.g. Ref. [6]), a few years ago devices became available showing patterns based on a superposition of a few tilted waves [7–10]. Quantitative information on the connection between wavenumber and detuning was not given and the predicted scaling behavior (1) was not checked. A scaling like (1) was obtained for vertical-cavity regenerative amplifiers [18]. However, no threshold behavior was found for the off-axis emission and hence at least some part of the signal results from linear scattering. Furthermore, we are not aware of any investigation in a non-semiconductor laser but nice work was done in photorefractive oscillators, where a configuration similar to a plano-planar one was mimicked by a suitable combination of intra-cavity focusing elements [19, 20].

In this paper, we study the relationship between wavenumber and detuning conditions in broad-area VCSELs in a quantitative way and compare it to theoretical calculations. Due to the complex longitudinal cavity structure of a VCSEL, the calculation of the phase shifts is more involved than implied by (1), although it turns out that this still serves as a suitable guideline.

2 Experiment

2.1 *Devices*

The devices used are similar to the ones described in Refs. [9, 10]. They are top emitters with a $40 \times 40\,\mu m^2$ aperture and are packaged in TO-type housings without caps. The active region consists of three $Al_{0.11}Ga_{0.89}As$ quantum wells with $Al_{0.36}Ga_{0.64}As$ barriers in between. The emission wavelength is around 780 nm. The active region is encased by $Al_{0.36}Ga_{0.64}As$ spacer layers with a thickness of λ (Fig. 2). The cavity is closed by two highly reflective distributed Bragg mirrors, consisting of 48 (bottom) and 31 (top) layers, respectively. The transitions between the high- and low-index layers is not abrupt but smoothed out in order to reduce the electrical resistance. A laterally oxidized layer above the active region provides current and optical confinement. The devices are electrically pumped with a low-noise dc current source.

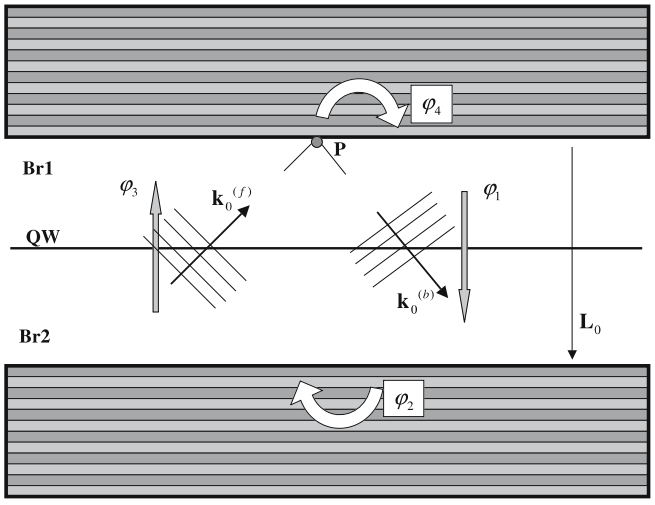

FIGURE 2 Schematic cavity structure of a VCSEL (see text) and illustration of the various phase shifts important in deriving the resonance condition. Starting from point ***P*** the light passes through the spacer layer and the active layer composed of quantum wells QW, acquiring the phase shift φ_1. φ_2, φ_4 are the phase shifts acquired at reflection from the Bragg reflectors Br1, Br2, φ_3 the one acquired during the backward transition through the spacer layer

The VCSEL is mounted on a heat sink. Its temperature is controlled and stabilized by a thermo-electrical element and a feedback circuit. The temperature of the heat sink can be adjusted between about 20 and $-20\,^\circ$C and is measured via a thermocouple. We note that the actual temperature of the active zone in the laser will be higher due to Joule heating from the pump current. It is well known that the detuning between the gain maximum and the cavity resonance depends on temperature, since both have a different temperature dependence (typical values are 0.28 nm/K for the gain maximum and 0.075 nm/K for the resonance; see e.g. Ref. [8]). Hence, temperature is a convenient control parameter to control the detuning condition and test the relationship in (1).

2.2 *Experimental setup*

In Fig. 3 the experimental setup is shown. The laser and an anti-reflection-coated aspherical collimating lens (numerical aperture 0.5) are placed into an air-tight box to avoid condensation. The collimated beam is then sent through polarization optics, i.e. a half-wave plate and a linear polarizer, which are used to select one of the two linear polarization states belonging to the principal axes of the VCSEL. This analyzing optics is followed by three detection arms: first, the aperture of the laser is imaged onto one-half of a high-resolution cooled charge-coupled device (CCD) camera (Apogee AP6-E, 1024×1024 pixels, 14-bit resolution) through an imaging lens and a stack of neutral density filters (near field). Second, the Fourier spectrum of the field is imaged onto the other half of the CCD camera (far field). Third, the beam is coupled via a multi-mode fibre into a spectrometer (0.05-nm resolution). Alternatively, some part of the beam is focused onto a low-bandwidth photodetector yielding a signal proportional to the output power.

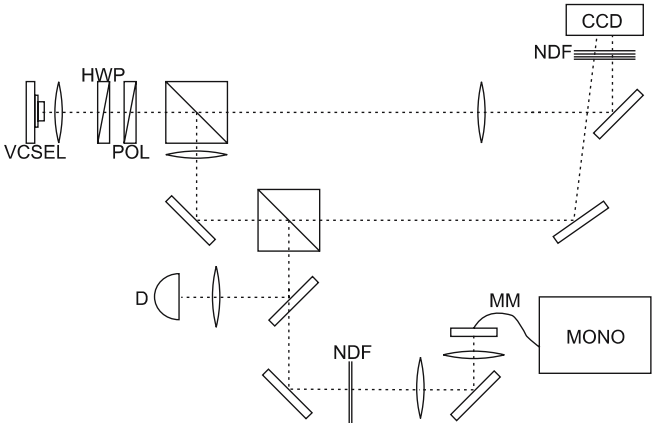

FIGURE 3 Scheme of the experimental setup (HWP = half-wave plate, POL = linear polarizer, NDF = neutral density filter, MM = multi-mode fiber, MONO = monochromator, D = photodetector). For further explanation see text

With this setup near-field, far-field and spectra can be observed simultaneously. The pixels in the far-field images are calibrated to divergence angles, or the wavenumbers in reciprocal microns, respectively, by measuring the divergence angle of the output beam directly for some modes in a different setup. The accuracy of this calibration is about $\pm 4\%$.

2.3 *Experimental results*

Figure 4 shows near-field and far-field images for a heat-sink temperature $T = -10.3\,^{\circ}\mathrm{C}$ and different currents I. The threshold current is about 16 mA at this temperature. As can be seen in Fig. 4a, the device starts lasing at a localized spot located at one corner of the aperture (the aperture is visible in light grey representing spontaneous emission). In the far field, the emission is centered around wavenumber zero.

If the current is increased, the next ignited mode consists of four strongly off-axis Fourier modes in the far field (plus a few side peaks), as can be seen in Fig. 4b. The emission angle is approximately 24°. In the near field, this corresponds to a kind of wavy stripe pattern with a very short wavelength (about 0.93 m) and some additional larger-scale modulation perpendicular to the stripes. We mention that this larger-scale modulation indicates the onset of localization of the emission pattern along classical rays being reflected at the boundaries of the laser. These 'coherent states of quantum billiards' exist in a limited (though robust) current interval starting slightly above threshold for even lower temperatures [9, 10].

If the current is increased further, more irregular patterns are excited represented by a ring with several stronger Fourier modes on it and elongated spots closer to the beam center (not shown in the figure). At even higher values of the current the variety of excited patterns grows and the far field shows more and more rings always separated by a distinct spacing (Fig. 4c).

We mention that the VCSEL is not linearly polarized but also emits in the orthogonal polarization component (with approximately equal power). The frequency shift between the two polarization components was measured for the on-axis spot to be 10 GHz, compatible with the birefringence values found in small-area lasers (see e.g. Ref. [21]). Details of the

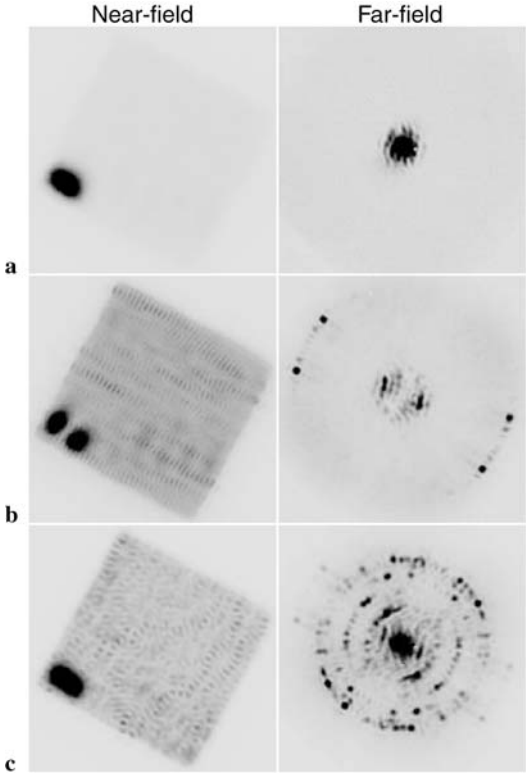

FIGURE 4 Near- and far-field images for $T = -10.3\,^{\circ}\mathrm{C}$ for dominant polarization. (**a**) 17 mA, (**b**) 20 mA, (**c**) 23 mA. The images are plotted in a linear grey scale where 'black' denotes high intensity

patterns are different, but the general features and wave-vector dependences agree. For the strongly off-axis wave vectors in the patterns consisting of a low number of wave vectors (Fig. 4b), we also observe the tendency described in Refs. [7, 8] that the polarization vector is orthogonal to the wave vector (see Ref. [17] for an explanation). Since we are mainly interested in the wavenumber dependences, we present only one polarization component here.

Figure 5 shows similar measurements for $T = 18.3\,^{\circ}\mathrm{C}$, i.e. near room temperature. The threshold lies at about 11 mA. Obviously the wavenumbers of excited patterns at this temperature are lower than for $T = -10.3\,^{\circ}\mathrm{C}$. The emission always stays around the beam center in Fourier space and the near-field pattern is never as regular as in Fig. 4b. (We will analyze the temperature dependence of the wavenumbers quantitatively below.) For both measurements, and in fact for almost the complete temperature range, the localized spot appears first at threshold. Afterwards, the outermost wave vector is excited close to threshold. With increasing current the number of excited modes grows, but the wavenumbers stay within the boundaries set by the first mode. Also, the wavenumber of a specific mode stays constant with changing current.

Similar results are obtained in other devices that do not show the localized spot at room temperature, although the existence of the latter is quite common in these devices. We will comment on possible origins below. Although the existence of this spot is obviously not a desirable property for a laser, we will see below that it is actually advantageous for our present purposes.

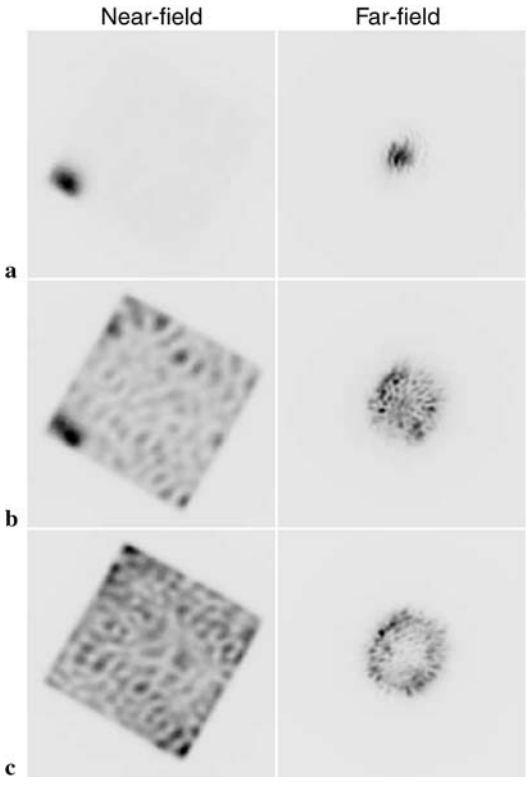

FIGURE 5 Near- and far-field images for $T = 18.3\,^{\circ}\mathrm{C}$ for dominant polarization. (**a**) 12 mA, (**b**) 15 mA, (**c**) 18 mA

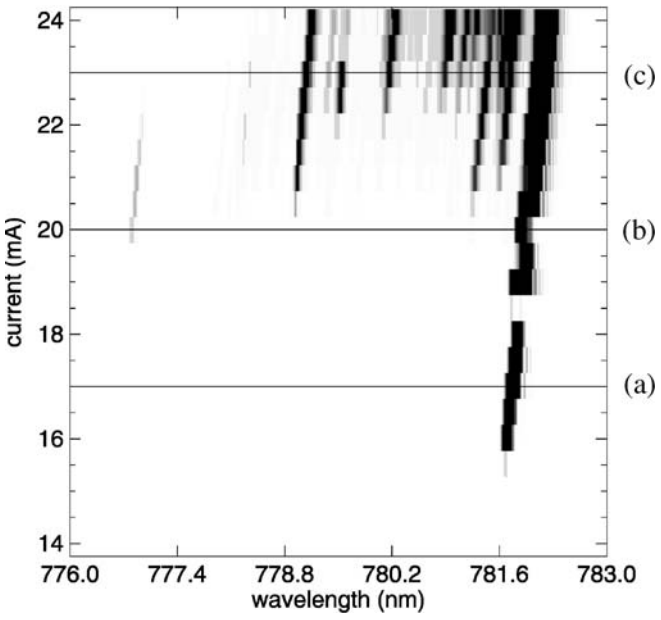

FIGURE 6 Contrast-enhanced optical spectra for $T = -10.3\,^{\circ}\mathrm{C}$ for different currents. 'Black' denotes high intensity. The lines marked with (**a**), (**b**) and (**c**) correspond to the images in Fig. 4

At room temperature, some 'filamentary' emission dominated by a single spot was also reported at threshold in Refs. [7, 8] (see Fig. 3b of Ref. [7]). For low temperature these observations agree in the appearance of wavy stripe patterns related to the emission of a far field dominated by four peaks (see also Refs. [9, 10]). A transition to multi-mode patterns with several rings in the far field for increasing current was also found. Hence, our findings present a confirmation of these seminal results on pattern formation in VCSELs in devices of different origin, thus illustrating the robustness of the phenomena.

The fact that different kinds of patterns are observed for different operating conditions (irregular states consisting of a lot of wave vectors are emitted at high temperature, whereas states with a low number of well-defined wave vectors prevail at lower temperature) and devices (with or without a localized spot) indicates that the observed structures result from a complicated interplay of nonlinearities, boundary conditions and inhomogeneities. However, an understanding of these effects is beyond the scope of the present paper.

For further investigation, the spectrum of the laser emission was recorded with the spectrometer. The resulting spectra are plotted in dependence on current. In Fig. 6 such a plot is shown for $T = -10.3\,^{\circ}\mathrm{C}$. Several lines with a distinct slope can be seen, each with a different threshold. On the far right, the most prominent line corresponds to the nearly on-axis emission of the laser on the localized spot. It displays two gaps where the emission changes polarization locally. On the far left the line corresponding to the four Fourier modes in Fig. 4b is apparent, but very weak in intensity. Note that the absolute intensities of the lines do not necessarily represent the intensity of the mode in the beam on a quantitative level, since the coupling efficiency for the off-axis modes to the fiber is somewhat smaller than for on-axis modes and very sensitive to alignment.

The spectrum has a width of around 4 nm or 2 THz once the off-axis modes are excited. Hence, one can expect local dynamics on the time scale of about 500 fs. This is far below the time resolution of our measurement system and actually with the spatial resolution desired even nowadays quite a challenge and probably unavailable, at least in two spatial dimensions. Hence, the images shown represent time averages. The complex spatio-temporal dynamics of semiconductor lasers was addressed in several theoretical papers (see e.g. Refs. [22, 23]) but only a few experiments are available [24, 25]. The fact that a distinct pattern survives even after time averaging is often referred to as 'symmetry on average' and is related to the boundary conditions [23, 26–28].

Although the spectrum is heavily multi-mode and the dynamics is seemingly complex, we make use of the fact that the modes are still well separated in Fourier space as well as in the optical spectra to establish a correspondence between individual modes in the two kinds of spectra.

The first observation is that all lines exhibit a constant slope that is equal for all wavelengths and was determined to be 0.071 nm/mA. The shift in wavelength with current is due to Joule heating in the laser: the increase in temperature pushes the resonance of the laser cavity and the maximum of the gain curve towards higher wavelengths. We also measured the wavelength shift in the spectra in dependence on temperature, which is also the same for all modes (0.062 nm/K). Using these two values, the shift of temperature with current could be inferred indirectly (1.1 K/mA). With this number the approximate effective temperature in the cavity can be calculated from heat-sink temperature and driving current. The fact that all modes shift the same with temperature implies that the

detuning between different modes does not depend on temperature. This is important, since we do not need to include the temperature dependence of the refractive index in the theoretical treatment.

Equation (1) relates a phase shift or detuning to wavenumber. To infer the detuning of the emission from the longitudinal resonance is usually a difficult task in a laser, since the emission of a laser is self-sustained and there is no external reference (in contrast to, for example, a driven cavity; see Refs. [19, 20] for the approaches taken there). This is why the localized emission spot in the laser is helpful: it marks the wavelength of the on-axis mode and thus gives an indication of the position of the longitudinal resonance (see below). Thus, we plot the wavenumber of a mode against the difference of its wavelength and the wavelength of the spot. Putting together the results for different temperatures (between 20 and $-20\,^{\circ}$C) we obtain the data displayed in Fig. 7 (solid squares). The errors for the transverse wavenumber result mainly from the conversion of pixels to reciprocal m in the far-field images. The errors for the detuning result from the uncertainty in the spectrometer measurements and from interpolation of wavelengths.

As expected from the qualitative discussion of Figs. 4 and 5, the wavenumber increases with increasing detuning (decreasing temperature due to the different thermal shifts of gain and resonance). The data suggest a square-root-like dependence, as expected from (1). This is verified by plotting the data in a double-logarithmic scale (see the inset in Fig. 7). The slope of the linear fit shown there is 0.497 ± 0.008 (excluding the three most deviating points for low detuning; the quoted uncertainty as given by the linear regression routine), 0.502 ± 0.008 (excluding the two most deviating points for low detuning) and 0.56 ± 0.05 (taking all data points into account). Since the data points at low detuning are the ones where the measurement uncertainties in detuning and wavenumber have the largest impact, one can conclude that the measurements confirm the square-root-like scaling excellently.

The observations suggest the interpretation of the outermost short-wavelength peak of the spectrum as the gain maximum, where the laser wants to operate. There is even a rather good quantitative agreement: the expected change of detuning is about 0.2 nm/K. The data represent a range of about 40 K. Hence, we expect a change of the preferred wavelength by about 8 nm, which is not too far from the 6.5 nm we observe.

Finally, we comment on the error we possibly make by assuming that the wavelength of the 'spot' corresponds to the longitudinal resonance. Obviously, the emission is not homogeneous and thus will be shifted to the blue of the exact resonance condition. For beams with a Gaussian shape, this shift is given by the so-called Gouy phase; see e.g. Ref. [29]. We measure a radius of $w_0 = 3.4\,\mu$m in the near field (half-width at $1/e^2$-point of intensity) and of $k_\perp = 0.69\ \mathrm{m}^{-1}$ in the far field. It is shown in Ref. [30] that the latter value should also give the effective wavenumber yielding the same phase shift for a tilted wave as the Gouy phase of the Gaussian beam. This value is smaller than the lowest wavenumber where we could obtain reasonable data for the radius of the ring. In addition, the dependence of wavenumber on detuning is rather steep around zero detuning. Hence, we consider the error to be certainly smaller than 0.5 nm. This value is also consistent with an estimate for the 'detuning zero' condition obtained by assuming the validity of a quadratic scaling as in (1) and fitting the function $k_\perp^2 = p_1(\Delta - \Delta_0)$ (Δ detuning in nm, Δ_0 error in detuning, ideally zero, p_1 additional fit parameter) to the data. From this, $\Delta_0 = (-0.05 \pm 0.01)$ nm is obtained, which is of the order of the uncertainty in the measurement of the wavelength and is consistent with the assumption that the 'spot' marks the position of the cavity resonance reasonably well.

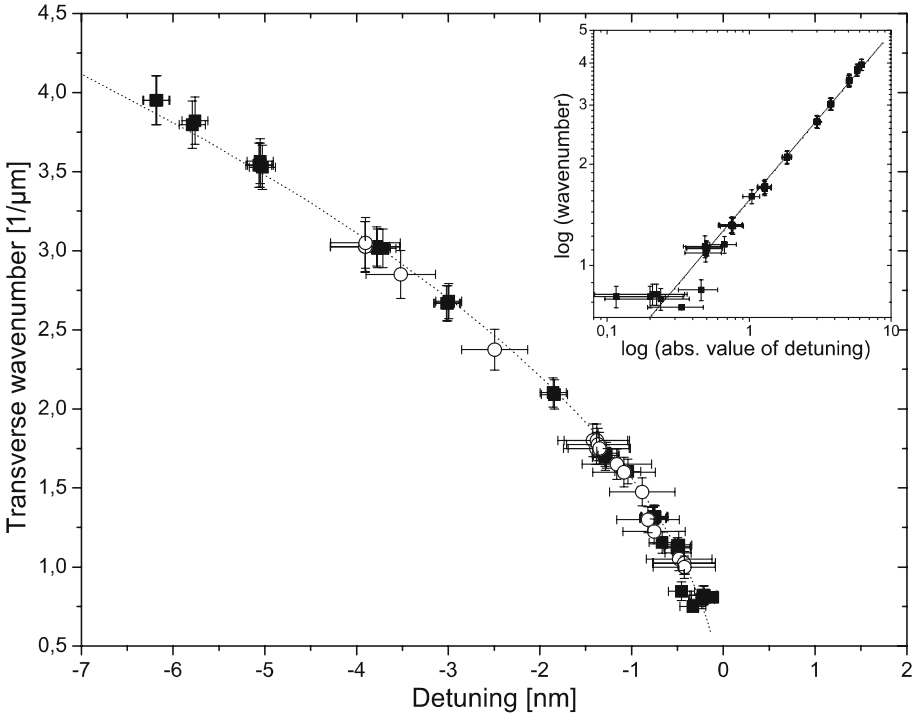

FIGURE 7 Dependence of the transverse wave number on detuning (see text). *Inset* shows experimental data in double-logarithmic scale with linear fit (excluding the three *data points* with the largest deviations for low values of the detuning). The *dotted line* in the main figure is a square-root function with the parameters derived from the fit to the log–log data. The data points are derived from both polarization components. The *solid squares* denote data from a device with a localized emission spot, the *open circles* data from a device without such a spot

We remark that the origin of the spot is not clear. The near-field intensity below threshold is rather homogeneous (leveling off slightly towards the perimeter of the device) and there is no enhancement of the spontaneous emission at the position where the spot appears at higher currents. Since the near field intensity distribution below threshold is not necessarily a good image of the carrier distribution because the amplified spontaneous emission is strongly filtered by the cavity, we also investigated the spatial distribution of the spontaneous emission escaping on the low-wavelength side of the Bragg stop band ($\lambda < 760\,\mathrm{nm}$) by imaging the near field through an interference filter. The spontaneous emission shows an enhancement at the perimeter and especially in the corners of the device. An enhancement of the carrier density at the perimeter is known to occur in top-emitting VCSELs due to current crowding at the oxide aperture (see e.g. Ref. [4]). However, there is no noticeable difference between the emission in the four corners, which might explain the preference of the device to emit at that particular spot. Thus, the emission of the spot does not seem to be related directly to a strong inhomogeneity in current injection. A possible explanation might be some inhomogeneity with increased non-radiative combination and hence local heating. The resulting thermal lens creates locally a stable cavity and the device might operate on that. Obviously, this implies a small frequency shift, but this is exactly what we addressed in the paragraph above. However, this explanation is speculative.

For completeness, we also checked the scaling characteristics for a device which does not show a localized spot. In this device, only the wavenumber versus emission wavelength is directly available from measurements. However – similar to that discussed above – an estimation of the wavelength of the longitudinal resonance λ_0 can be obtained by fitting the function $k_\perp^2 = p_1(\lambda_0 - \lambda)$ to the data, where $k_\perp$ and λ are the measured wavenumbers and emission wavelengths (the latter had to be corrected obviously for the wavelength shift due to the temperature change) and p_1 an additional fit parameter. The value of λ_0 obtained was used to convert the measured emission wavelengths to detuning values and the resulting data points were added to Fig. 7 (open circles). The fact that they fit nicely the data from the other laser is a further confirmation of the consistency of the assumptions.

3 Theory

3.1 *Phase-matching conditions for VCSEL cavity*

The most rigorous treatment of the wavelength selection in a laser is based on a linear stability analysis of the non-lasing zero-amplitude state at lasing threshold (assuming some suitable dynamical model), and the frequency of the excited tilted mode is determined as the imaginary part of the eigenvalue of the unstable eigenmode undergoing an Andronov–Hopf bifurcation [31]. However, it often turns out to be sufficient to consider the resonance conditions of the 'cold' cavity, i.e. the cavity without pumping (leading, for example, to (1) for a simple Fabry–Perot cavity model). Below, we apply this approach to a VCSEL, i.e. a Fabry–Perot cavity closed by Bragg reflectors.

Figure 2 shows the considered scheme of the VCSEL cavity. We consider plane waves with $\boldsymbol{k} = (k_x, k_y, k_z)$ as eigenfunctions, which is exactly valid if the laser has an infinite aperture. A pair of transverse Fourier modes with $(k'_x, k'_y) = -(k_x, k_y)$ is still an exact solution of the eigenvalue problem in a laser with a rectangular aperture, if the field is fully reflected at the boundaries (i.e. has no evanescent tail), although the resulting spectrum is discrete ($k_x = m\pi/d$, $k_y = m'\pi/d$, d size of aperture, $m, m' = 0, 1, \ldots$), of course, in this case. Note that this assumption was also invoked in order to explain the quantum billiard patterns in Refs. [9, 10]. Often, it is assumed that the waveguiding due to the oxide aperture is smeared out along the whole cavity. The effective strength of this waveguide can be calculated by the so-called effective-index method [23, 32]. Due to the finiteness of the refractive-index jump, there will be some penetration of the field to the oxide region. The resulting shift in wavenumber and emission frequency can be calculated from the theory of dielectric slab waveguides (see e.g. Ref. [33]) in a straightforward way. Due to the large size of the devices considered, these shifts are small, e.g. for a rather small effective refractive index jump of $\Delta n = 0.026$ the shift of the $m = 1$ TE fundamental mode with respect to the longitudinal cavity resonance is only $-0.003\,\mathrm{nm}$ (for perfectly reflective boundary conditions it would be $-0.0031\,\mathrm{nm}$; for simplicity the frequency shift of the resonance is calculated here using the assumption that the reflection phase at the mirrors does not change with wavenumber). For higher mode orders, the shift becomes noticeable, although it is still rather small (e.g. for $m = 25$, corresponding to $k \approx 2\ \mathrm{m}^{-1}$, the difference between perfectly reflective boundary conditions and the $\Delta n = 0.026$ case is $0.03\ \mathrm{m}^{-1}$ in wavenumber and 0.06 nm in wavelength). However, it turns out that these shifts actually have no influence on the wavenumber versus detuning relationship, because the shifts happen in such a way that the corresponding values still lie on the wavenumber versus detuning curve for the infinite device. We will give an explanation below.

Obviously, there are more rigorous models available, which take more details of the transverse confinement in a VCSEL into account and extend up to full vectorial treatments of the complete longitudinal and transverse VCSEL structure (see e.g. Refs. [34, 35]). However, in the broad-area limit these models are first computationally too expensive (Debernardi [34, 35] considered only devices with a maximal diameter of 11 m) and second unnecessarily complex (see above).

The frequency ω of a pattern, which is characterized by some wave vector $\boldsymbol{k} = (k_x, k_y, k_z)$, can be obtained from the requirement that the overall phase shift of a plane wave with the corresponding $k = |\boldsymbol{k}|$ in the cavity must be equal to

$$\varphi(\boldsymbol{k}) \equiv \sum_{i=1}^{4} \varphi_i(\boldsymbol{k}) = 2\pi m\,, \tag{2}$$

where φ_1, φ_3 is the phase shift in two spacer layers and φ_2, φ_4 is the value of the phase shift after reflection from Bragg reflectors (see Fig. 2). The phase shift at the mirrors is often disregarded in determining the resonance frequencies because it is negligible and/or unimportant, but this can be different for microcavity structures such as VCSELs.

The integer number m is the same for all transverse modes or tilted waves belonging to the same longitudinal cavity mode with frequency ω_c. Therefore, it is convenient to present the frequency ω related to the wave vector $\boldsymbol{k}_\perp$ as

$$\omega = \omega_c + \Omega(\boldsymbol{k}_\perp)\,, \tag{3}$$

where the frequency detuning Ω depends on $\boldsymbol{k}_\perp$ and $\Omega(0) = 0$. Then, for a fixed value of $k_\perp = |\boldsymbol{k}_\perp|$, the wave vector is given by

$$\boldsymbol{k} = (k_z(\omega), \boldsymbol{k}_\perp) = (k_z(\Omega(k_\perp)), \boldsymbol{k}_\perp)\,, \tag{4}$$

where

$$k_z(\omega) = \sqrt{\frac{n^2(\omega)\omega^2}{c^2} - k_\perp^2}\,. \tag{5}$$

Note that (5) is valid for media homogeneous in the transverse directions as well as for waveguides. In the latter, the propagation constant $\beta(\omega)$ needs to replace $k_z(\omega)$. This however will not change the wavenumber versus detuning curve calculated below, but only which discrete values on this curve represent the boundary selected modes for a specific aperture size and strength of oxide confinement.

Taking this into account, (2) can be rewritten as

$$\Delta\varphi(k_\perp, \Omega) \equiv \sum_{i=1}^{4} \Delta\varphi_i(k_\perp, \Omega) = 0\,, \tag{6}$$

where $\Delta\varphi_i(k_\perp, \Omega) = \varphi_i(k_\perp, \Omega) - \varphi_i(0, 0)$.

In Table 1 the refractive indices are summarized, which are taken for an evaluation of the phase shifts for the structure under study. We compared three sources for the refractive indices [36–38], which yield close results (see table) in spite of some interpolations involved.

The phase shift of the field due to the reflection from the Bragg reflector can be obtained via a calculation of the reflectivity coefficient R using the transfer matrix approach:

$$R(\boldsymbol{k}) \equiv R(\Omega, \boldsymbol{k}_\perp) = |R(\Omega, \boldsymbol{k}_\perp))| \exp(\mathrm{i}s(\Omega, \boldsymbol{k}_\perp))\,. \tag{7}$$

Variable	Value
Spacer layer	
composition x ($Al_xGa_{1-x}As$)	0.36
refractive index (n_0)	3.42 ± 0.01
group index (n_{gr0})	4.18 ± 0.06
First Bragg layer	
composition x ($Al_xGa_{1-x}As$)	0.9
refractive index (n_1)	3.093 ± 0.01
group index (n_{gr1})	3.47 ± 0.01
Second Bragg layer	
composition x ($Al_xGa_{1-x}As$)	0.3
refractive index (n_2)	3.46 ± 0.01
group index (n_{gr2})	4.46 ± 0.08

TABLE 1 Structure of VCSEL cavity

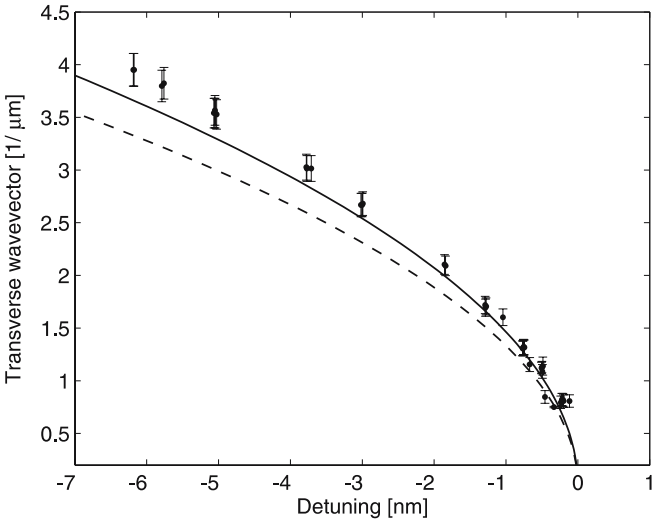

FIGURE 8 Dependence of transverse wave number $k_\perp$ on the wavelength calculated using (6)–(9) taking into account dispersion (*solid line*) and without dispersion (*dashed line*)

So, the phase shift for Bragg reflectors is

$$\Delta\varphi_2(\Omega, \boldsymbol{k}_\perp) = \Delta\varphi_4(\Omega, \boldsymbol{k}_\perp) = s(\Omega, \boldsymbol{k}_\perp)\,. \tag{8}$$

We take here the same phase shift for the top and bottom Bragg reflectors, since the result is practically independent of the number of layers when this number is considerably large, as in the devices used in the experiments. In principle, the reflection also depends on the direction of $\boldsymbol{k}$ with respect to the polarization axis of the field. Although this effect might be important for polarization selection [17, 39], it was checked that it does not give any visible impact on the result for the length-scale selection.

The phase shift of the field due to propagation in the spacer layer is

$$\Delta\varphi_1(\Omega, \boldsymbol{k}_\perp) = \Delta\varphi_3(\Omega, \boldsymbol{k}_\perp) = L_0(k_z - k_c)\,. \tag{9}$$

Equation (6) with (8) and (9) is an implicit function of Ω. The resulting relationship between emission wavelength and the square of the transverse wave number is shown in Fig. 8 (dashed line).

The relationship between $k_\perp$ and the detuning shows a square-like dependence demonstrating that the scaling relation (1) also holds for VCSELs. This is confirmed by the fact that the scaling exponent – determined in a log–log plot of the data – is 0.5 with an accuracy of at least 10^{-4}. In particular, this implies that the paraxial approximation (which was not invoked up until now) is still a good approach to describe the emission of the VCSEL (for the values of detuning considered). The experimentally measured value is completely compatible with this numerical finding. The absolute values are within a 30% range of the experimental values, i.e. they have the correct order of magnitude, although they are definitely smaller than the experimental measurements.

3.2 *Effects of dispersion*

It is known that semiconductor media are characterized by strong dispersion. So, we should take into account

the dependence of refractive indices on Ω. The frequency dependence of the index can be determined in a linear approximation by

$$n(\omega_c + \Omega) = n(\omega_c) + \left.\frac{dn}{d\omega}\right|_{\omega_c} \Omega \,, \tag{10}$$

where the derivatives are related to the group index n_{gr} by

$$\frac{dn}{d\omega} = \frac{n_{gr} - n(\omega_c)}{\omega_c} \,. \tag{11}$$

The resulting dependence of the transverse wavenumber on the detuning is shown in Fig. 8 by a solid line. Again, a square-root-like dependence is apparent (and confirmed by a fitting of the scaling exponent). The absolute values of the wavenumbers are higher than in the case without dispersion. Hence, the agreement between theoretical and experimental data improved considerably (about 15% mismatch for the high wavenumbers). This indicates that it is necessary to include dispersive effects for a quantitative description of the length scales, although the deviations are still somewhat larger than expected from the uncertainties of the refractive indices and the accuracy of the experimental measurements. It is obvious that the deviations increase for increasing detuning. The reason for that is not clear at the moment.

3.3 *Reduced description*

The data in Fig. 8 indicate that in the dependence of the phase shift on $k_\perp$ and Ω only the square and linear orders need to be considered, respectively. Therefore, in (6) we consider $k_\perp^2$ and Ω as small quantities, and expand the square-root term as

$$k_z(\Omega, k_\perp) \cong \frac{n_0}{c}\omega_c + \frac{1}{2}\frac{c}{n_0\omega_c}\left(\frac{n_0^2}{c^2}2\omega_c\Omega - k_\perp^2\right) \,. \tag{12}$$

In particular, this implies that the paraxial approximation is assumed. After some simplifications, (12) is reduced to

$$k_z(\Omega, k_\perp) \cong k_c + \frac{n_0^\star}{c}\Omega - \frac{1}{2k_c}k_\perp^2 \,, \tag{13}$$

where $n_0^\star = n_0$ represents the phase index of the spacer layer, if dispersion is not taken into account, and $n_0^\star = n_{gr0}$ represents the group index of the spacer layer, if dispersion is taken into account.

Substituting (13) into (6), one obtains

$$\Omega\tau_0 - \frac{L_0}{2k_c}k_\perp^2 = -s(\Omega, k_\perp) \,, \tag{14}$$

where $\tau_0 = n_0^\star L_0/c$ is the time delay in the spacer layer with thickness L_0. Equation (14)) is still implicit because of the complicated dependence of the Bragg phase shift s on Ω. In a next step, the phase shift due to the Bragg reflector is expanded into a Taylor series around the point $(\Omega, k_\perp) = (0, 0)$:

$$s(\Omega, k_\perp) = \frac{\partial s}{\partial\Omega}\Omega + \frac{1}{2}\frac{\partial^2 s}{\partial k_\perp^2}k_\perp^2 + \ldots \,. \tag{15}$$

Inserting this decomposition into (14), one finds that

$$\Omega\left(\tau_0 + \frac{\partial s}{\partial\Omega}\right) - k_\perp^2\left(\frac{L_0}{2k_c} - \frac{1}{2}\frac{\partial^2 s}{\partial k_\perp^2}\right) = 0 \,. \tag{16}$$

Equation (16) can be written as

$$\frac{\Omega\tau_e}{2} = \frac{L_d}{2k_c}k_\perp^2 \,. \tag{17}$$

Here,

$$L_d = L_0 - k_c\frac{\partial^2 s}{\partial k_\perp^2} \tag{18}$$

denotes a diffraction equivalent length, i.e. the distance which leads to the same diffractive phase shift as the spacer layer plus the Bragg mirrors. From a diffraction point of view, a cavity of length L_d closed by two 'normal' mirrors (i.e. mirrors where the reflection phase does not depend on the transverse wavenumber of the incident light) would be identical to a VCSEL cavity. The contribution due to the Bragg mirror in this expression was introduced before in Ref. [40] as a diffraction equivalent distance and the result agrees within an accuracy of 1% with ours (based on numerical evaluation).

It is worth noting that this definition does not depend on the presence of dispersion, because the dispersion introduces a linear phase shift which is proportional to frequency. The effect of dispersion enters in the effective cavity round-trip time,

$$\tau_e = 2\left(\tau_0 + \frac{\partial s}{\partial\Omega}\right) \,. \tag{19}$$

The expression for the deviation between $\tau_e/2$ and τ_0 coincides with the reflection delay at frequency ω_c introduced in Ref. [41]. This reflection delay is associated with a phase penetration depth of the light into the Bragg reflector, which was defined in the same work as the distance at which a normal mirror needs to be placed to provide the same reflection phase shift for the wave as the Bragg reflector. A similar definition was also used in Refs. [33, 42]. Since dispersion (in paraxial approximation) also introduces a linear contribution to the overall phase shift, (19) remains correct if dispersion is taken into account. Then, we can define an effective cavity length,

$$L_e = \frac{c\tau_e}{2n_{gr0}} \,. \tag{20}$$

It is important to note that L_e is not equivalent to L_d. This implies that it is not possible to replace directly a VCSEL cavity by a simpler equivalent cavity with $L = L_e$ for $k_\perp \neq 0$. However, an equivalent cavity (with a reflection phase of zero at the mirrors) can be mimicked by assuming that is it filled with a material with a suitably modified refractive index $\tilde{n}_{gr0}$, i.e. by demanding that

$$L_d \equiv \tilde{L}_e = \frac{c}{\tilde{n}_{gr0}}\left(\tau_0 + \frac{\partial s}{\partial\Omega}\right) \,. \tag{21}$$

4 Conclusion

In this paper, we confirmed experimentally a scaling relationship – a linear dependence of the square of the wavenumber on the detuning between emission wavelength and cavity resonance – predicted for laser patterns in a plano-planar resonator in a VCSEL. This scaling is typical for patterns in nonlinear optical systems and is directly related to the structure of the paraxial wave equations. Hence, it does not only apply to nonlinear resonators but also to single-mirror feedback systems [43, 44] and counterpropagating beams in longitudinally extended media [45].

Taking into account the longitudinal cavity structure of the VCSEL and dispersion, there is a good qualitative agreement between experiment and theory, if dispersion is taken into account. Thus, the results give confidence to tackle now more complex spatio-temporal phenomena like nonlinear mode interaction and the resulting dynamics. It appears that the observed structures result from a complicated interplay of nonlinearities, boundary conditions and inhomogeneities. In particular, it would be interesting to gain more insight as to why irregular states consisting of a lot of wave vectors are emitted at high temperatures, whereas states with a low number of well-defined wave vectors prevail at lower temperatures, and how these states finally give way to the coherent states of quantum billiards [9, 10] for even lower temperatures.

ACKNOWLEDGEMENTS The work of M.S.-R. and T.A. was supported by the Deutsche Forschungsgemeinschaft by money for equipment and a studentship. The German–Belorussian collaboration is supported also by travel grants of the Deutsche Forschungsgemeinschaft. The German–Taiwanese cooperation is supported by the Deutsche Akademische Austauschdienst and the Taiwanese National Science Council. We are very grateful to W. Lange for fruitful discussions and support over the last years.

REFERENCES

1 W.W. Chow, K.D. Choquette, M.H. Crawford, K.L. Lear, G.R. Hadley, IEEE J. Quantum Electron. **33**, 1810 (1997)
2 M.B. Willemsen, M.U.F. Khalid, M.P. v. Exter, J.P. Woerdman, Phys. Rev. Lett. **82**, 4815 (1999)
3 D. Wiedenmann, R. King, C. Jung, R. J er, R. Michalzik, P. Schnitzer, M. Kicherer, K.J. Ebeling, IEEE J. Sel. Top. Quantum Electron. **5**, 503 (1999)
4 M. Grabherr, M. Miller, R. J er, R. Michalzik, U. Martin, H.J. Unold, K.J. Ebeling, IEEE J. Sel. Top. Quantum Electron. **5**, 495 (1999)
5 R.A. Morgan, K. Kojima, T. Mullally, G.D. Guth, M.W. Focht, R.E. Leibenguth, M.T. Asom, Appl. Phys. Lett. **61**, 1160 (1992)
6 H. Li, T.L. Lucas, J.G. McInerney, R.A. Morgan, Chaos Soliton. Fract. **4**, 1619 (1994)
7 S. Hegarty, G. Huyet, J.G. McInerney, K.D. Choquette, Phys. Rev. Lett. **82**, 1434 (1999)
8 S.P. Hegarty, G. Huyet, P. Porta, J.G. McInerney, K.D. Choquette, K.M. Geib, H.Q. Hou, J. Opt. Soc. Am. B **16**, 2060 (1999)
9 K.F. Huang, Y.F. Chen, H.C. Lai, Y.P. Lan, Phys. Rev. Lett. **89**, 224 102 (2002)
10 Y.F. Chen, K.F. Huang, H.C. Lai, Y.P. Lan, Phys. Rev. Lett. **90**, 053 904 (2003)
11 L.A. Lugiato, R. Lefever, Phys. Rev. Lett. **58**, 2209 (1987)
12 M. Tlidi, M. Georgiou, P. Mandel, Phys. Rev. A **48**, 4605 (1993)
13 P.K. Jakobsen, J.V. Moloney, A.C. Newell, R. Indik, Phys. Rev. A **45**, 8129 (1992)
14 W.J. Firth, A.J. Scroggie, Europhys. Lett. **26**, 521 (1994)
15 J. Lega, J. Moloney, A. Newell, Phys. Rev. Lett. **73**, 2978 (1994)
16 M.C. Cross, P.C. Hohenberg, Rev. Mod. Phys. **65**, 851 (1993)
17 N.A. Loiko, I.V. Babushkin, J. Opt. B: Quantum S. O. **3**, S234 (2001)
18 T. Ackemann, S. Barland, J.R. Tredicce, M. Cara, S. Balle, R. J er, P.M. Grabherr, M. Miller, K.J. Ebeling, Opt. Lett. **25**, 814 (2000)
19 U. Bortolozzo, P. Villoresi, P.L. Ramazza, Phys. Rev. Lett. **87**, 274 102 (2001)
20 A. Esteban-Martin, J. Garcia, E. Roldán, V.B. Taranenko, G.J. de Valcárcel, C.O. Weiss, Phys. Rev. A **69**, 033 816 (2004)
21 M.P. v. Exter, A.K.J. v. Doorn, J.P. Woerdman, Phys. Rev. A **56**, 845 (1997)
22 O. Hess, Opt. Express **2**, 424 (1998)
23 T. Rössler, R.A. Indik, G.K. Harkness, J.V. Moloney, Phys. Rev. A **58**, 3279 (1998)
24 I. Fischer, O. Hess, W. Elsäßer, E. Göbel, Europhys. Lett. **35**, 579 (1997)
25 A. Barchanski, T. Gensty, C. Degen, I. Fischer, W. Els er, IEEE J. Quantum Electron. **39**, 850 (2003)
26 L. Ning, Y. Hu, R.E. Ecke, G. Ahlers, Phys. Rev. Lett. **71**, 2216 (1993)
27 B.J. Gluckman, P. Marq, J. Bridger, J.P. Gollub, Phys. Rev. Lett. **71**, 2034 (1993)
28 J. Farjas, D. Hennequin, D. Dangoisse, P. Glorieux, Phys. Rev. A **57**, 580 (1998)
29 A.E. Siegman, *Lasers* (University Science Books, Mill Valley, CA 1986)
30 T. Ackemann, W. Grosse-Nobis, G.L. Lippi, Opt. Commun. **189**, 5 (2001)
31 A.C. Newell, J.V. Moloney, *Nonlinear Optics* (Addison-Wesley, Redwood City, CA 1992)
32 G.R. Hadley, Opt. Lett. **20**, 1483 (1995)
33 L.A. Coldren, S.W. Corzine, *Diode Lasers and Photonic Integrated Circuits* (Wiley, New York 1995)
34 P. Debernardi, Phys. Rev. A **63**, 1 (2001)
35 P. Debernardi, G.P. Bava, C. Degen, I. Fischer, W. Els er, IEEE J. Quantum Electron. **38**, 73 (2002)
36 K.F. Huang, personal communication (2004)
37 E.F. Schubert, http://www.rpi.edu/∼schubert/Educational %20resources/Materials%20-%20refractive%20index%20and %20extinction%20coefficient.pdf
38 S. Adachi, J. Appl. Phys. **58**, R1 (1985)
39 J.V. Moloney, personal communication (2001)
40 D.I. Babic, Y. Chung, N. Dagli, J.E. Bowers, IEEE J. Quantum Electron. **29**, 1950 (1993)
41 D.I. Babic, S.W. Corzine, IEEE J. Quantum Electron. **28**, 514 (1992)
42 K.J. Ebeling, in *Semiconductor Quantum Optoelectronics: From Quantum Physics to Smart Devices*, ed. by A. Miller, M. Ebrahimzadeh, D.M. Finlayson (SUSSP Publications and Institute of Physics Publishing, Bristol, 1999), pp. 295–338
43 G. D'Alessandro, W.J. Firth, Phys. Rev. Lett. **66**, 2597 (1991)
44 T. Ackemann, W. Lange, Appl. Phys. B **72**, 21 (2001)
45 W.J. Firth, C. Pare, Opt. Lett. **13**, 1096 (1990)